EUROPEAN ORGANISATION FOR NUCLEAR RESEARCH (CERN)

Submitted to: JHEP

CERN-EP-2023-002
31st January 2023

Search for long-lived, massive particles in events with displaced vertices and multiple jets in pp collisions at $\sqrt{s}$ = 13 TeV with the ATLAS detector

The ATLAS Collaboration

A search for long-lived particles decaying into hadrons is presented. The analysis uses 139 fb^{-1} of pp collision data collected at $\sqrt{s}$ = 13 TeV by the ATLAS detector at the LHC using events that contain multiple energetic jets and a displaced vertex. The search employs dedicated reconstruction techniques that significantly increase the sensitivity to long-lived particles decaying in the ATLAS inner detector. Background estimates for Standard Model processes and instrumental effects are extracted from data. The observed event yields are compatible with those expected from background processes. The results are used to set limits at 95% confidence level on model-independent cross sections for processes beyond the Standard Model, and on scenarios with pair-production of supersymmetric particles with long-lived electroweakinos that decay via a small R-parity-violating coupling. The pair-production of electroweakinos with masses below 1.5 TeV is excluded for mean proper lifetimes in the range from 0.03 ns to 1 ns. When produced in the decay of $m(\tilde{g})$ = 2.4 TeV gluinos, electroweakinos with $m(\tilde{\chi}_1^0)$ = 1.5 TeV are excluded with lifetimes in the range of 0.02 ns to 4 ns.

1 Introduction

The interest in searches for long-lived particles (LLPs) has recently grown and they have become an important part of the hunt for new physics at the Large Hadron Collider (LHC). LLPs appear in a variety of models trying to address fundamental puzzles of the Standard Model (SM) of particle physics and yield a large palette of signatures at colliders that inspires a diverse and ambitious search programme at the LHC [1, 2].

There are various mechanisms by which particles can obtain significant lifetimes ($\gtrapprox$ 10 ps) in beyond the Standard Model (BSM) theories. The decays of such particles can be suppressed in so-called Hidden Valley models where large barrier potentials reduce the rate of kinematically allowed decays [3]. Decays happening via a highly virtual intermediate state, or in highly compressed mass spectra can also result in long lifetimes [4, 5]. Finally, long-lived particles also appear in models with small couplings, such as those often found in R-parity-violating supersymmetry (SUSY) [6], as happens for the simplified models used as a benchmark for the search presented here.

SUSY [7–12] models have the potential to achieve gauge-coupling unification, provide an explanation for dark matter, and alleviate the naturalness problem [13–16]. In the minimal supersymmetric extension to the SM (MSSM) [17, 18], R-parity-violating (RPV) couplings that violate baryon-number and lepton-number conservation naturally occur at tree level. The RPV terms of the MSSM superpotential are given by

$$\mathcal{W}_{\text{RPV}} = \mu_i \ell_i h_u + \lambda_{ijk} \ell_i \ell_j \bar{e}_k + \lambda'_{ijk} \ell_i q_j \bar{d}_k + \lambda''_{ijk} \bar{u}_i \bar{d}_j \bar{d}_k,$$

where μ_i, λ_{ijk}, λ'_{ijk}, and λ''_{ijk} are the RPV couplings, ℓ and e represent the lepton and charged-lepton supermultiplets, h_u represents the up-type Higgs supermultiplets, and q, u, and d represent the quark, up-type quark, and down-type quark supermultiplets [6]. The symbols i, j, and k are generation indices.

The search presented in this paper targets small values of the λ'' couplings, assuming all other RPV couplings to be exactly zero. Several low- and intermediate-energy experimental observations constrain the value of the RPV couplings to be small [19, 20]. This naturally leads to suppression of the decay processes and can give rise to long-lived SUSY particles. A nonzero λ'' coupling allows the electroweakinos, supersymmetric states that arise from the mixing of the superpartners of the $U(1)_Y$, $SU(2)_L$ and Higgs fields, to decay into three quarks. Two different signal scenarios are used as benchmarks in this analysis. The Electroweak (EWK) RPV scenario, shown in Figure 1(a), considers the associated production of the lightest charged and neutral electroweakinos, that is, $\tilde{\chi}_1^{\pm}\tilde{\chi}_1^0$, $\tilde{\chi}_1^{+}\tilde{\chi}_1^{-}$, $\tilde{\chi}_2^0\tilde{\chi}_1^0$ and $\tilde{\chi}_1^{\pm}\tilde{\chi}_2^0$, assuming pure-higgsino states. In the Strong RPV scenario, shown in Figure 1(b), pairs of gluinos $\tilde{g}$, the superpartners of the SM gluons, are produced. Each $\tilde{g}$ promptly decays with a 100% branching ratio to a SM quark–antiquark pair and a neutralino $\tilde{\chi}_1^0$, the lightest neutral electroweakino. The electroweakinos in both models decay with a 100% branching ratio via the λ'' couplings to light-flavour quarks.

This paper presents the first search for the RPV models described above in events with a massive, multi-track displaced vertex and multiple energetic jets using proton–proton collisions collected by the ATLAS experiment at a centre-of-mass energy of $\sqrt{s}$ = 13 TeV. Dedicated track and vertex reconstruction algorithms are employed to maximize the reconstruction and selection efficiency of displaced vertices originating from LLP decays which occur inside of the tracking volume but at a discernible distance from the interaction point of the incoming beams. The analysis does not require that the jets are linked to the displaced vertex in order to retain sensitivity to various BSM decay topologies. Signal region (SR) criteria are designed to select on the order of one background event in the available data sample, while maximizing

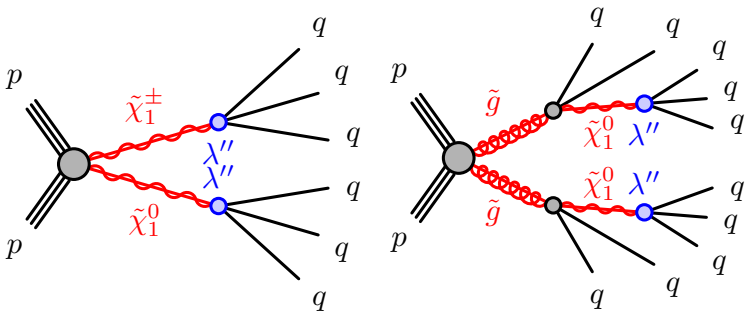

Figure 1: Diagrams showing production of a (a) chargino-neutralino pair ($\tilde{\chi}_1^{\pm}\,\tilde{\chi}_1^0$) and (b) a gluino pair ($\tilde{g}\tilde{g}$), in which each gluino decays into a pair of quarks and a long-lived neutralino ($\tilde{\chi}_1^0$). The $\tilde{\chi}_1^{\pm}$ and $\tilde{\chi}_1^0$ decay into three quarks via the R-parity-violating coupling λ''. For sufficiently small values of λ'', the lifetime of the $\tilde{\chi}_1^{\pm}$ and $\tilde{\chi}_1^0$ becomes long enough to cause decays which are significantly displaced from their production points.

the expected signal yield. The predictions of the background yields from several sources are entirely derived from data, with individual contributions estimated from dedicated control regions (CRs).

Similar searches were performed previously by the ATLAS and CMS collaborations at $\sqrt{s} = 7, 8$ and 13 TeV [21–26]. This analysis significantly expands the limits given by previous ATLAS searches [23]. Novel techniques to estimate background processes that can produce a displaced vertex signal were developed, and sensitivity to RPV SUSY models predicting production of long-lived electroweakinos is demonstrated for the first time.

2 ATLAS detector

The ATLAS detector [27, 28] at the LHC is a multipurpose particle detector with a forward–backward symmetric cylindrical geometry and a near 4π coverage in solid angle.[1] It consists of an inner tracking detector (ID) surrounded by a thin superconducting solenoid providing a 2 T axial magnetic field, electromagnetic (EM) and hadron calorimeters, and a muon spectrometer. The inner tracking detector covers the pseudorapidity range $|\eta| < 2.5$. It consists of silicon pixel, silicon microstrip (SCT), and transition radiation tracking (TRT) detectors. The pixel detector has four barrel layers and three disks in each of the forward and backward regions. The barrel layers surround the beam pipe at radii of 33.3 mm, 50.5 mm, 88.5 mm, and 122.5 mm, covering $|\eta| < 1.9$. The pixel detector spans the radius range from 3 cm to 12 cm, the SCT spans 30 cm to 52 cm, and the TRT spans 56 cm to 108 cm.

Lead/liquid-argon (LAr) sampling calorimeters provide EM energy measurements with high granularity. A steel/scintillator-tile hadron calorimeter covers the central pseudorapidity range $|\eta| < 1.7$. The endcap and forward regions are instrumented with LAr calorimeters for both the EM and hadronic energy measurements up to $|\eta| = 4.9$. The muon spectrometer surrounds the calorimeters and is based on three large air-core toroidal superconducting magnets with eight coils each. The field integral of the toroids ranges between

[1] ATLAS uses a right-handed coordinate system with its origin at the nominal interaction point (IP) in the centre of the detector and the z-axis along the beam pipe. The x-axis points from the IP to the centre of the LHC ring, and the y-axis points upwards. Cylindrical coordinates (r, ϕ) are used in the transverse plane, ϕ being the azimuthal angle around the z-axis. The pseudorapidity is defined in terms of the polar angle θ as $\eta = -\ln\tan(\theta/2)$.

2 T m and 6 T m across most of the detector. The muon spectrometer includes a system of precision tracking chambers and fast detector chambers for triggering. A two-level trigger system is used to select events [29]. The first-level trigger is implemented in hardware and uses a subset of the detector information to reduce the accepted rate to at most 100 kHz. This is followed by a software-based trigger that reduces the accepted event rate to 1 kHz on average depending on the data-taking conditions. An extensive software suite [30] is used for real and simulated data reconstruction and analysis, for operation, and in the trigger and data acquisition systems of the experiment.

3 Data and simulated event samples

Proton—proton collision data recorded by the ATLAS detector between 2015 and 2018 are used for this analysis. In this period, the LHC delivered colliding beams with an average number of pp interactions per bunch crossing of 33.7. After applying beam, detector, and data-quality criteria [31] the total integrated luminosity of the data is 139 fb^{-1}. The uncertainty in the combined 2015–2018 integrated luminosity is 1.7%, obtained using the LUCID-2 detector for the primary luminosity measurements [32, 33].

The data were recorded using a combination of triggers requiring multiple energetic jets with transverse momentum p_{T} thresholds that depend on the jet multiplicity. These ranged from four jets with $p_{\mathrm{T}} > 100$ GeV to seven jets with $p_{\mathrm{T}} > 45$ GeV.

Monte Carlo (MC) simulated event samples are used to aid the estimate of background from SM processes and to model the targeted signal models. The matrix element (ME) calculation for the SUSY production processes was performed to leading-order precision with MadGraph5_aMC@NLO 2.6.2 [34] interfaced to Pythia 8.212 [35] for parton showering (PS) and hadronization. All other SUSY-particle contributions are assumed to be decoupled. The ME calculation was performed at tree level and included the emission of up to two additional partons for all signal samples. The parton distribution function (PDF) set used for the generation of the signal samples was NNPDF2.3lo [36] with the A14 [37] set of tuned underlying-event and shower parameters. The ME–PS matching was performed with the CKKW-L prescription [38, 39], with a matching scale set to one quarter of the produced SUSY particle mass. The electroweakino production cross sections were computed at next-to-leading-order (NLO) plus next-to-leading-log (NLL) precision [40–44] in a limit of mass-degenerate higgsinos $\tilde{\chi}_2^0$, $\tilde{\chi}_1^{\pm}$, and $\tilde{\chi}_1^0$. The nominal cross-section and the uncertainty were taken from an envelope of cross-section predictions using different PDF sets and factorization and renormalization scales, as described in Ref. [45]. Signal cross-sections for the gluino pair production were calculated to approximate Next-to-Next-to-Leading-Order (NNLO) in the strong coupling constant, adding the resummation of soft gluon emission at Next-to-Next-to-Leading-Log (NNLL) accuracy (approximate NNLO +NNLL) [46–53]. The nominal cross-section and its uncertainty were derived using the PDF4LHC15_mc PDF set, following the recommendations of Ref. [54]. In the electroweakino case, the cross-sections ranged from 300 ± 10 fb at $\tilde{\chi}_1^0$ mass of 300 GeV to 21.5 ± 3.7 ab at 1700 GeV, assuming pure-higgsino states. In the gluino case, they ranged from 8.9 ± 1.4 fb at a $\tilde{g}$ mass of 1.6 TeV to 46 ± 14 ab at 2.6 TeV.

Samples of multijet events were generated using Pythia 8.230 with leading-order matrix elements for dijet production which were matched to the parton shower. The NNPDF2.3lo PDF set was used in the ME generation, the parton shower, and the simulation of the multi-parton interactions. The A14 set of tuned parameters was used. These samples are used for an independent closure test of the data-driven background estimates.

To simulate the effects of additional pp collisions in the same and nearby bunch crossings (pile-up), additional interactions were generated using the soft QCD processes provided by Pythia 8.186 with the A3 tune [55] and the MSTW2008LO PDF set [56], and overlaid onto each simulated hard-scatter event. The MC samples were reweighted so that the pile-up distribution matches the one observed in the data. The MC samples were processed through an ATLAS detector simulation [57] based on Geant4 [58]. All MC samples were reconstructed in the same manner as the data.

4 Event reconstruction

The signal processes targeted by this search include massive particles with mean proper lifetimes τ up to $O(10)$ ns. Several charged decay products will originate from locations in the detector with a substantial displacement from the primary proton–proton interaction and require dedicated techniques to be efficiently reconstructed.

The standard ATLAS track reconstruction algorithm is optimized for charged particles originating from the interaction region, or from decays of short-lived particles such as b-hadrons. Constraints are set on the transverse and longitudinal impact parameters of track candidates relative to the interaction region ($|d_0| < 10$ mm and $|z_0| < 250$ mm, respectively), and their hit multiplicities in order to reduce the computational complexity. These selections result in inefficiencies in the reconstruction of tracks with large impact parameters, corresponding to charged particles produced in the LLP decays. To reconstruct these tracks, a dedicated track reconstruction, called *large-radius tracking* (LRT) [59], is performed. This reconstruction step takes as input the hits left over from the standard tracking procedure and applies looser requirements, in particular on the transverse and longitudinal impact parameters ($|d_0| < 300$ mm and $|z_0| < 1500$ mm). Tracks from the standard processing and the LRT processing are treated collectively in all subsequent steps of reconstruction.

Collision vertices (CV) are reconstructed [60] with at least two associated tracks that are consistent with originating from the beam collision region in the x–y plane. For each reconstructed vertex the quantity Σ_{p_T}, defined as the sum of squared transverse momenta of associated tracks, is computed. The primary vertex (PV) in the event is the vertex with the highest Σ_{p_T}.

A dedicated secondary-vertex reconstruction algorithm for LLP decays is employed to reconstruct displaced vertices (DVs) [61]. As input to this vertex reconstruction, only tracks with transverse momentum $p_\mathrm{T} > 1$ GeV and which satisfy several additional requirements on the number and distribution of the associated hits in the tracking detectors are considered. The vertexing starts by forming two-track seed vertices, where at least one track in each two-track seed vertex must have $|d_0| > 2$ mm. Tracks used to seed vertex formation are called *selected tracks*. The two-track seed vertices are then iteratively merged to form n-track vertices. Ambiguities due to tracks being compatible with more than one vertex are resolved by comparing their χ^2 values in the vertex fits, or by merging the vertices if the distance between their estimated positions is not significant enough. As a final step, additional tracks satisfying looser selection criteria are attached to the reconstructed vertices in order to recover inefficiencies from the vertex seeding selection. These tracks are referred to as *attached tracks* and have looser hit selection requirements than selected tracks. The resulting DV reconstruction efficiency, defined as the probability for a true neutralino decay to be matched with a reconstructed DV as a function of the radial position R, and the total vertex selection efficiency are shown in Figure 2, highlighting the improvements due to LRT and attached tracks. The efficiency degrades rapidly beyond 300 mm due to a requirement on the minimum number of hits ($N_\mathrm{hits} \geq 7$) applied in the LRT algorithm. The drop in efficiency at small radii is a result of the $|d_0|$

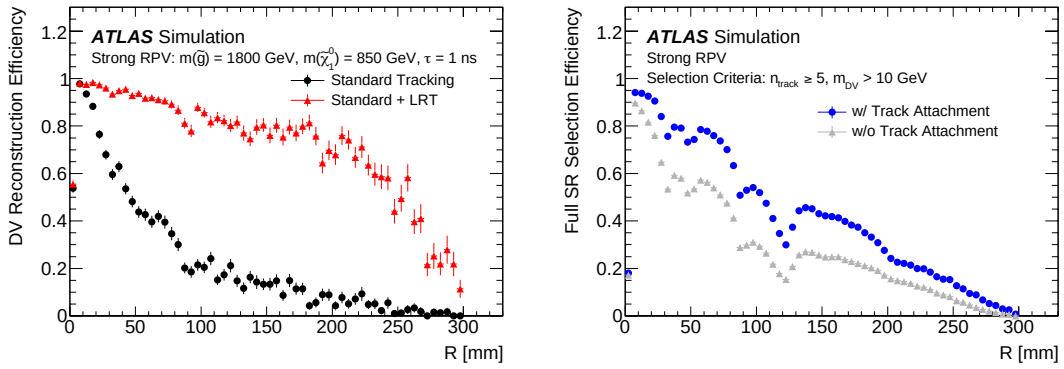

(a) (b)

Figure 2: In (a), the DV reconstruction efficiencies with and without the special LRT processing are shown for the Strong RPV model with $m(\tilde{g}) = 1800$ GeV $m(\tilde{\chi}_1^0) = 850$ GeV and $\tau(\tilde{\chi}_1^0) = 1.0$ ns. The efficiency is defined as the probability for a true neutralino decay with at least two charged decay products with $p_{\mathrm{T}} > 1$ GeV and $|\eta| < 5$ to be matched with a reconstructed DV. In (b), the impact of attached tracks on the total SR selection efficiency is shown, which is defined in Section 5. The total SR selection efficiency is calculated using a combined sample of simulated Strong RPV signal events with $m(\tilde{g}) = 1.6 - 2.6$ TeV $m(\tilde{\chi}_1^0) = 50 - 1550$ GeV and $\tau(\tilde{\chi}_1^0) = 0.01 - 10.0$ ns.

requirement on the two-track seed vertices. Larger neutralino masses lead to more high-p_{T} particles being produced in the decay, which increase the reconstruction efficiency of the DV.

While electrons and muons are not used in the event selection in this search, they are used in a procedure to remove overlapping objects and define the final collection of jets. Muon candidates are reconstructed in the region $|\eta| < 2.7$ from MS tracks matching ID tracks. Candidate muons are required to have $p_{\mathrm{T}} > 10$ GeV and satisfy the *medium* identification requirements defined in Ref. [62], based on the number of hits in the different ID and MS subsystems, and on the ratio of the charge and momentum (q/p) measured in the ID and MS divided by the sum in quadrature of their corresponding uncertainties.

Electron candidates are reconstructed from isolated electromagnetic calorimeter energy deposits matched to ID tracks and are required to have $|\eta| < 2.47$, a transverse momentum $p_{\mathrm{T}} > 10$ GeV, and to satisfy the *LooseAndBLayer* requirement defined in Ref. [63], which is based on a likelihood using measurements of shower shapes in the calorimeter and track properties in the ID as input variables. Electrons which share an ID track with a muon are discarded.

Jets are reconstructed from three-dimensional energy clusters in the calorimeters [64] using the anti-k_t jet clustering algorithm [65, 66] with a radius parameter $R = 0.4$. Only jet candidates with $p_{\mathrm{T}} > 20$ GeV and $|\eta| < 2.8$ are considered. Jets are calibrated using MC simulation with corrections obtained from in situ techniques [67]. Events are discarded if they contain any jet with $p_{\mathrm{T}} > 20$ GeV not satisfying basic quality selection criteria designed to reject detector noise and non-collision backgrounds by imposing the *BadLoose* cleaning selection, described in Ref. [68], without the cuts on the fraction of jet energy deposited within the electromagnetic calorimeter and the jet charged-fraction. Jets within an angular distance $\Delta R = \sqrt{(\Delta\eta)^2 + (\Delta\phi)^2} = 0.2$ of an electron candidate are discarded.

A second collection of jets is reconstructed to aid in estimating the SM background by exploiting the track density in an event. These jets, referred to as track-jets, are constructed with an anti-k_t algorithm with $R = 0.4$ using all tracks with $p_{\mathrm{T}} > 1$ GeV and $|d_0| < 2$ mm. In contrast to the jet reconstruction algorithm from calorimeter energy deposits, the track jet reconstruction is not sensitive to displaced LLP decays,

due to the selection on the tracks $|d_0|$. In order to take into account the effects arising from the presence of pile-up interactions, track-jets are reconstructed for each collision vertex in the event. Before track jet-finding, each track is matched with only one reconstructed collision vertex to minimize the probability of clustering together tracks which originate from different interactions into a single jet. The matching proceeds as follows: first, tracks are assigned with a collision vertex if their longitudinal impact parameter significance satisfies $|z_0/\sigma_{z_0}| < 3$ relative to that vertex. Second, any remaining unassociated tracks are assigned to a collision vertex if their longitudinal impact parameter satisfies $|z_0| < 0.5$ mm relative to that vertex. If a track is found to be compatible with multiple collision vertices, then the vertex with the highest Σ_{p_T} is chosen. Track-jet finding is then done for each collision vertex. Track-jets are retained for further analysis if their p_T satisfies $p_T > 20$ GeV.

5 Event selection

The LRT reconstruction algorithm used in this search is computationally expensive and so it was not run on all events recorded with the ATLAS detector. Instead, a selection referred to as a *filter* is applied to the events satisfying the trigger conditions described in Section 3. The events passing the filter requirements compose a special data stream that is processed with the LRT algorithm. This analysis uses two filters which apply a selection on uncalibrated jets: the *Trackless jet* and the *High-p_T jet* filters. The Trackless jet filter targets the electroweakino pair production signals and the High-p_T jet filter targets the gluino pair production signals. The Trackless jet filter selects events with a high multiplicity of jets (> 3) satisfying p_T thresholds ranging from 45 to 100 GeV. Furthermore, events are required to have at least one Trackless jet with $p_T > 70$ GeV and $|\eta| < 2.5$, or at least two Trackless jets with $p_T > 50$ GeV and $|\eta| < 2.5$. A jet is considered trackless if the sum of the transverse momenta of all standard (non-LRT) tracks associated with the jet is less than 5 GeV. The High-p_T jet filter selects events with a high multiplicity of jets (> 3) satisfying p_T thresholds ranging from 75 to 220 GeV. There is no requirement on the presence of Trackless jets in the High-p_T jet filter.

An offline jet p_T selection is applied after jet calibration. The specific choices are made for the p_T thresholds to ensure a full efficiency of the offline event selection relative to the trigger and filter requirements. These thresholds depend on the jet multiplicity and range from 55 to 137 GeV for the events passing the Trackless jet filter and from 90 to 250 GeV for the events passing the High-p_T jet filter.

Candidate events are required to have at least one reconstructed collision vertex and satisfy the High-p_T jet or Trackless jet selection requirements.

DVs passing the baseline selection must be reconstructed with a high goodness-of-fit, $\chi^2/n_{\mathrm{DoF}} < 5$, to reject fake vertices. The reconstructed vertex must be within a fiducial region, which has an outermost boundary defined as $R_{\mathrm{DV}} = \sqrt{x_{\mathrm{DV}}^2 + y_{\mathrm{DV}}^2} < 300$ mm and $|z_{\mathrm{DV}}| < 300$ mm. In addition, the DV must be at least 4 mm away from any collision vertex in the transverse plane, both to avoid confusing the DV with one of those vertices and also to reduce the heavy flavour background which could contaminate the signal. To reduce background from hadronic interactions, DVs must satisfy a *material map* veto, which rejects DVs which have a reconstructed position consistent with the position of detector material. The material map, shown in Figure 3, is constructed using the known positions of detector elements and from the positions of low-mass vertices reconstructed in data. The material map veto removes 48% of the fiducial volume.

DVs passing the full selection must have at least five tracks, two of which must be selected tracks and a reconstructed invariant mass m_{DV} greater than 10 GeV. The m_{DV} is calculated from the four-momenta of

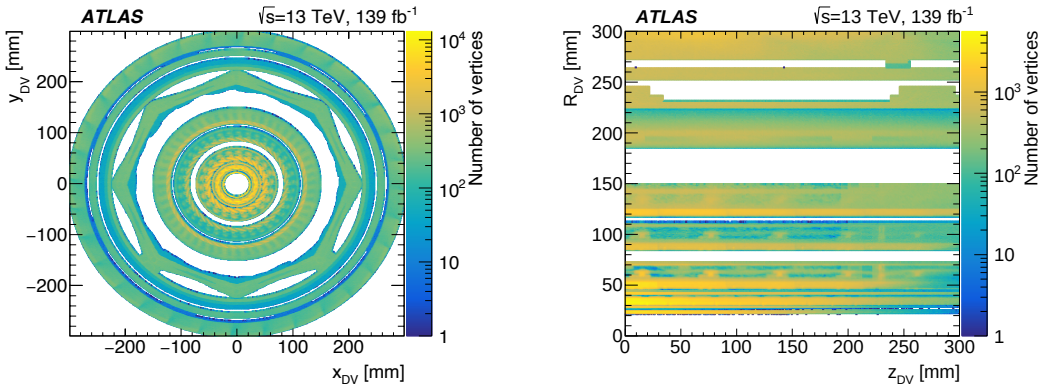

(a) (b)

Figure 3: The positions in the (a) $x-y$ plane and (b) $r-z$ plane of reconstructed displaced vertices that are vetoed by the material map in the analyzed data sample. The right figure is restricted to positive z values for presentation. The innermost area corresponds to the beampipe. This is surrounded by four pixel detector layers. The octagonal shape and outermost structures are due to support structures separating the pixel and SCT detectors.

Table 1: Summary of the track cleaning selections used for signal DV candidates. The track d_0-significance is given by $|d_0|/\sigma(d_0)$.

	Region	$0 < R_{\text{DV}} < 25$ mm	$25 < R_{\text{DV}} < 145$ mm	$R_{\text{DV}} > 145$ mm
Attached tracks	Track p_{T} [GeV]	> 2	$> 3^{\dagger}$	> 4
	Track d_0-significance	> 10	> 15	–
	$\Delta\phi_{\text{PV–DV}}$	$< \pi/2$		
	Upstream veto	No hits allowed with $R < R_{\text{DV}}$		
Selected tracks	Track p_{T} [GeV]	> 2	$> 2^{\dagger}$	> 2
	Track d_0-significance	> 10	–	> 10
	Upstream veto	No hits allowed with $R < R_{\text{DV}}$		

† this requirement is tightened to $p_{\text{T}} > 4$ GeV for tracks with $\Delta\phi_{\text{PV–DV}} < 0.2$

the tracks, assuming each track was produced by a charged pion. Only tracks satisfying specific quality selections, summarized in Table 1, are used in the calculation of the DV track multiplicity and mass. The selection criteria are designed to reject background DVs in the signal regions, while maintaining a high efficiency for signal vertices. As the background composition changes in different parts of the detector, these selections depend on R_{DV}, with different criteria before and after the beampipe ($R = 25$ mm) and the last pixel layer ($R = 145$ mm). Further requirements, aimed at rejecting wrong track-to-vertex associations, are applied on the azimuthal difference $\Delta\phi_{\text{PV–DV}}$ between the track direction and the vector connecting the primary vertex to the displaced vertex.

This analysis uses two mutually exclusive signal regions, as defined in Table 2. The High-p_{T} jet SR selects events that satisfy the High-p_{T} jet selection. The Trackless jet SR selects events which fail to satisfy the High-p_{T} jet selection but do satisfy the Trackless jet selection. Both SRs require at least one DV passing the full selection.

Table 2: Summary of the signal region selections. The x in the $n^{x}_{\text{jet/Trackless jet}}$ notation refers to the jet p_{T} threshold in GeV. All jets are required to have $|\eta| < 2.5$. The selection on $|\vec{R}_{DV} - \vec{R}_{CV}|$ considers all CVs in the event.

Signal Region	High-p_{T} jet SR	Trackless jet SR
Jet selection	$n^{250}_{\text{jet}} \geq 4$ or $n^{195}_{\text{jet}} \geq 5$ or $n^{116}_{\text{jet}} \geq 6$ or $n^{90}_{\text{jet}} \geq 7$	Fail High-p_{T} jet selection, $n^{137}_{\text{jet}} \geq 4$ or $n^{101}_{\text{jet}} \geq 5$ or $n^{83}_{\text{jet}} \geq 6$ or $n^{55}_{\text{jet}} \geq 7$, $n^{70}_{\text{Trackless jet}} \geq 1$ or $n^{50}_{\text{Trackless jet}} \geq 2$
DV preselection	$R_{\text{DV}} < 300$ mm, $\lvert z_{\text{DV}}\rvert < 300$ mm, $\min(\lvert\vec{R}_{\text{DV}} - \vec{R}_{\text{CV}}\rvert) > 4$ mm, $\chi^2/n_{\text{DoF}} < 5$, $n^{\text{DV}}_{\text{Selected tracks}} \geq 2$, satisfy material map veto	
$n^{\text{DV}}_{\text{Tracks}}$	≥ 5	
m_{DV}	>10 GeV	

The total efficiency of the high-p_{T} jet SR for selecting generated events in the EWK RPV model ranges from 20% to 70% for $m(\tilde{\chi}^0_1) = 500$ GeV to $m(\tilde{\chi}^0_1) = 1.7$ TeV and $\tau(\tilde{\chi}^0_1) = 0.1$ ns. For the Strong RPV model, the total efficiency of the high-p_{T} jet SR ranges from 50% to 80% for $m(\tilde{\chi}^0_1) = 200$ GeV to $m(\tilde{\chi}^0_1) = 1250$ GeV with $m(\tilde{g}) = 2.6$ TeV and $\tau(\tilde{\chi}^0_1) = 0.1$ ns. The total efficiency of the Trackless jet SR ranges from 7% to 40% for the EWK RPV model with $m(\tilde{\chi}^0_1) = 300$ GeV to $m(\tilde{\chi}^0_1) = 700$ GeV and $\tau(\tilde{\chi}^0_1) = 0.1$ ns, and does not have significant sensitivity to the Strong RPV model. Selection efficiency of both of the signal regions decreases for samples with neutralinos with shorter or longer lifetimes, due largely to the fiducial volume acceptance.

6 Backgrounds

There are no high-mass SM particles which produce displaced decays which satisfy the selections required in this search. Searches for displaced, multi-track vertices benefit from a small background which is caused predominantly by low-mass vertices being merged together and misclassified as a high-mass vertex. The backgrounds arise from instrumental and algorithmic effects and can be described by three main sources: hadronic interactions, accidental crossings, and merged vertices.

Hadronic interactions arise from particles interacting with the nuclei of detector material while traveling through the detector. If multiple charged particles are produced in this interaction, then they may be reconstructed as a displaced vertex. Due to the kinematics of this process, the charged particles resulting from the interaction are typically collimated, giving rise to relatively low-mass displaced vertices. Rare interactions occurring in less collimated decay products may result in a high-mass displaced vertex. The bulk of these DVs are localized in the material-dense regions of the detector and are removed by the material map veto. The residual background is due to hadronic interactions in the less dense regions of the detector or those that evade the material map veto due to the resolution of the vertex position or due to inefficiencies in the material map. This background class also includes vertices created by regular long-lived SM particles decaying in their natural decay mode. As the mass of long-lived particles in the SM are light ($\lessapprox 5$ GeV), these decays typically result in low-mass reconstructed vertices.

Low-mass displaced vertices that are crossed by an unrelated track are referred to as *accidental crossings*. A low-mass DV may be misclassified as a high-mass DV with higher track multiplicity if an unrelated track passes sufficiently close to the vertex to be attached to it during reconstruction. These tracks frequently form a large angle with the other tracks in the low-mass SM vertices they cross, resulting in a large increase in the invariant mass of the vertex.

The last category, merged vertices, considers the cases when two or more low-mass displaced vertices occur in the vicinity of each other. In these cases, the vertexing algorithm may mistakenly include them in the same vertex. This may increase the mass of the displaced vertex to the signal region. Vertices from decays of long-lived SM particles, hadronic interactions, or accidental crossings may be merged by the vertexing algorithm, resulting in a high-mass DV that satisfies the signal region selection.

Backgrounds are estimated by using an inclusive data-driven technique that predicts the rate of DVs from all three sources above. This method is described in Section 6.1 and validated in Section 6.2. Additionally, an alternative estimate is presented in Section 6.3 that is used to predict the three different sources of backgrounds separately and produce estimates for their distribution in the reconstructed mass of the DV. This method is used as additional validation and its results are compatible with the inclusive method. Furthermore, the alternative estimate is used to evaluate a systematic uncertainty on the inclusive method as described in Section 7.

6.1 Inclusive background estimation

The background estimation used in this analysis relies on the assumption that in a multijet final state, DV production is correlated to the presence of jets. All three sources of background DVs are correlated with track density, and the track density is correlated with the presence of jets in the event. Track-jets are chosen to maximize this correlation.

The method relies on the measurement of the probability that a SR-like DV is produced in proximity of a track jet in a statistically independent event selection from the SR. The probability is measured in a control region of data and is split into two parts. The first part, p_{DV}, is parameterized as a function of track jet properties and the second part, an extrapolation factor f, is defined inclusively. The extrapolation factor takes into account differences in the DV mass and track multiplicity requirements in the CR and in the SR. The p_{DV} is used to assign a weight to track-jets in events passing the SR jet selections. The sum of the weighted track-jets, multiplied by the extrapolation factor f, is taken as the total number of events with a background DV expected in the SR.

To study the correlation between DVs and track-jets in data, a control region is designed which contains track-jets but which also limits the contamination from signal models of interest. The CR is populated with data events collected using a single photon trigger, requiring an energetic photon with $E_{\mathrm{T}} > 140$ GeV. This trigger is selected because it does not alter the flavour composition of jets in the CR relative to those in the signal region. Events in the CR must fail to satisfy the jet selection requirements of both signal regions. Finally, events in the CR must have at least three track-jets with $p_{\mathrm{T}} > 20$ GeV. There is negligible signal contamination in this CR from the two simplified models considered in this search.

The jet-DV probability is parameterized as a function of both the track jet p_{T} and track multiplicity $N^{\mathrm{jet}}_{\mathrm{trk}}$ to take into account residual differences between the CR and the SRs. The fraction of events in the CR which contain a preselected DV with $m_{\mathrm{DV}} > 3$ GeV and $n^{\mathrm{DV}}_{\mathrm{Tracks}} > 2$ as a function of track jet multiplicity is shown in Figure 4(a). Events with more track-jets are found to be more likely to contain a DV. The proximity of

a DV and a track jet is calculated with $\Delta R_{\mathrm{DV,jet}} = \sqrt{\Delta\eta^2 + \Delta\phi^2}$ where $\Delta\eta$ and $\Delta\phi$ are measured between the PV–DV direction and the jet axis. The average $\Delta R_{\mathrm{DV,jet}}$ as a function of the DV track multiplicity is shown in Figure 4(b). DVs with a higher track multiplicity tend to be produced in closer proximity to track-jets, which is a sign that DVs which are more SR-like ($n^{\mathrm{DV}}_{\mathrm{Tracks}} \geq 5$) have a stronger correlation to track jet activity.

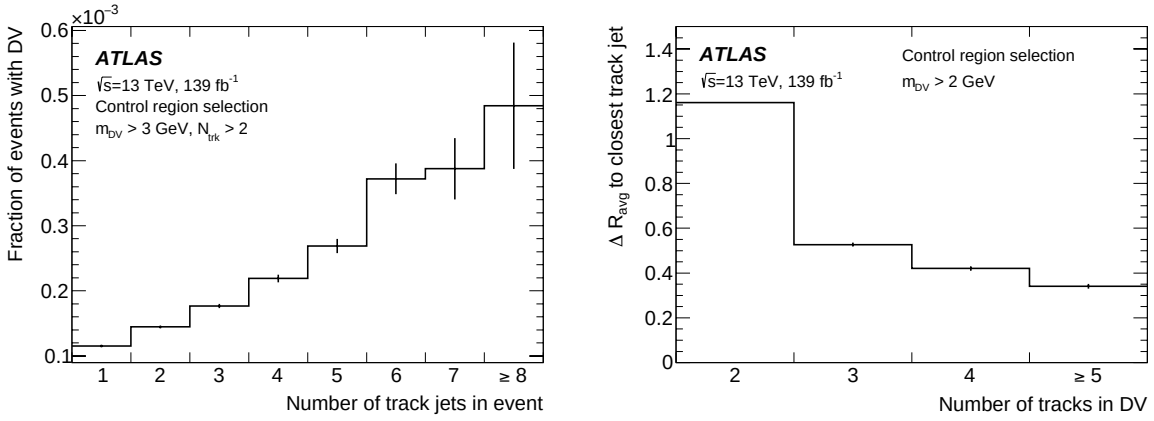

(a) (b)

Figure 4: In (a), the fraction of events in the CR with a reconstructed DV satisfying $m_{\mathrm{DV}} > 3$ GeV and $n_{\mathrm{Tracks}} > 2$ is shown. In (b), the average distance of DVs with $m_{\mathrm{DV}} > 2$ GeV to the closest track jet in the event is shown, as a function of n_{Tracks}.

The SR-like DVs in the CR are matched to the closest track jet in the event using $\Delta R_{\mathrm{DV,jet}}$. Each DV is matched to only one track jet in each event, and the DV position is not required to be within the jet. More than 70% of DVs are within the $\Delta R = 0.4$ cone of the nearest track jet. The ΔR distribution is stable as a function of DV mass, but shifts to lower values as the track multiplicity increases.

The jet-DV probability is computed as the ratio of the number of track-jets with a matched DV over the total number of track-jets in the CR. All DVs in the CR satisfying $n^{\mathrm{DV}}_{\mathrm{Tracks}} > 3$ and $m_{\mathrm{DV}} > 5$ GeV are considered for the determination of p_{DV}. The DV mass and track multiplicity requirements in the CR are looser than the SR-DV requirements so that there is adequate statistical precision in the CR to calculate the jet-DV probability. The jet-DV probability is found to range between 6×10^{-7} and 2×10^{-6}, with a mild dependence on the track jet p_{T} and $N^{\mathrm{jet}}_{\mathrm{trk}}$.

In events passing the High-p_{T} (Trackless) jet selections, each track-jet is assigned a weight which is equal to the corresponding p_{DV}, in order to estimate the number of background DVs expected in the High-p_{T} (Trackless) jet SR. The weighted sum is then multiplied by an additional extrapolation factor f which considers the difference between the DV mass and track multiplicity requirements used to calculate the jet-DV probability and in the SR selection. The extrapolation f is calculated by taking the ratio of the number of events with a reconstructed DV satisfying $n^{\mathrm{DV}}_{\mathrm{Tracks}} > 4$ and $m_{\mathrm{DV}} > 10$ GeV relative to the number of events with a reconstructed DV satisfying $n^{\mathrm{DV}}_{\mathrm{Tracks}} > 3$ and $m_{\mathrm{DV}} > 5$ GeV in the CR. The extrapolation f was determined to be 0.038 ± 0.022, where the uncertainty is propagated from the statistical variation of the number of events in the CR.

The method predicts respectively $0.46^{+0.27}_{-0.30}$ background events in the High-p_{T} jet SR and $0.83^{+0.51}_{-0.53}$ background events in the Trackless jet SR.

6.2 Validation of background model

Several statistically independent validation regions are defined and used to test the predictions of the background estimation method. Validation regions are defined in the SR sidebands by selecting events which pass the full signal region selection, except they contain at least one DV with $m_{\mathrm{DV}} < 10$ GeV or $n^{\mathrm{DV}}_{\mathrm{Tracks}} < 5$. A second set of validation regions is defined with events which pass all SR selections, but contain a high-mass DV that fails to meet the criteria of the material veto. For each validation region, a separate jet-DV probability is calculated from events in the CR. There are few events in the CR which satisfy the same DV selection criteria as the SR sideband validation regions with $n^{\mathrm{DV}}_{\mathrm{Tracks}} = 4$, $m_{\mathrm{DV}} > 10$ GeV and with $n^{\mathrm{DV}}_{\mathrm{Tracks}} \geq 5$, $5 < m_{\mathrm{DV}} < 10$ GeV. Therefore, the m_{DV} or $n^{\mathrm{DV}}_{\mathrm{Tracks}}$ requirements are loosened in order to calculate the jet-DV probability in a similar manner as the procedure performed for the estimate of background in the SR. The agreement between the background estimate and observed event counts in each of the validation regions is shown in Figure 5.

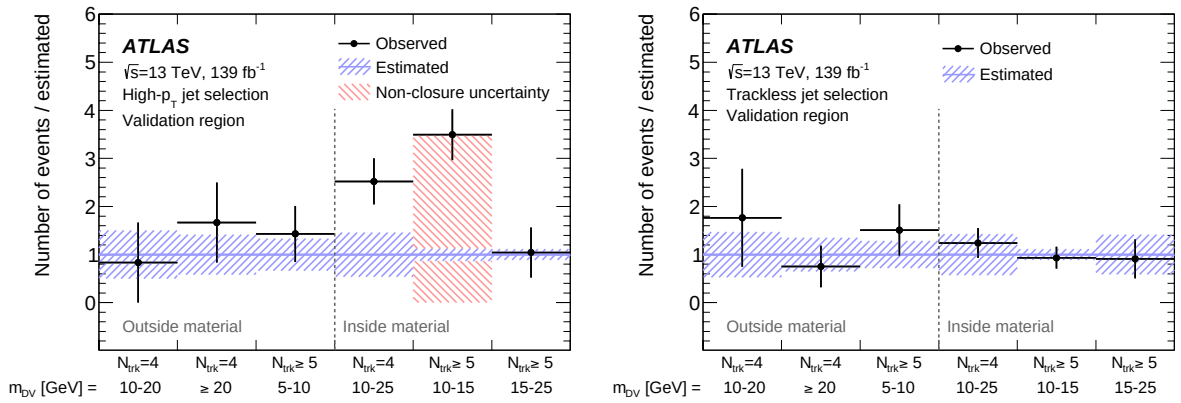

(a) (b)

Figure 5: Background estimates relative to expectations for (a) the High-p_{T} jet selection and (b) the Trackless jet selection showing validation regions with varying $n^{\mathrm{DV}}_{\mathrm{Tracks}}$ and m_{DV} requirements. Validation regions labeled *Outside (Inside) material* contain events with a displaced vertex which is accepted (rejected) by the material map veto requirement. The error band dashed with a positive slope includes all systematic uncertainties. The size of the non-closure uncertainty is shown by the band dashed with a negative slope, which is not propagated to the other validation regions in this figure.

Within uncertainties, good agreement is found between the background model and data in all of the SR sideband validation regions, as well as the inside material VRs for the Trackless jet selection. For events satisfying the High-p_{T} jet selection criteria inside of the material validation regions, there is a significant underestimation of the background in the $n^{\mathrm{DV}}_{\mathrm{Tracks}} = 4$, $10 < m_{\mathrm{DV}} < 25$ GeV and $n^{\mathrm{DV}}_{\mathrm{Tracks}} \geq 5$, $10 < m_{\mathrm{DV}} < 15$ GeV regions. These regions are significantly populated by hadronic interactions, which are expected to have a minimal contribution to the background in the signal region. The difference between the observed yields and the expectation from the background prediction in the $n^{\mathrm{DV}}_{\mathrm{Tracks}} \geq 5$, $10 < m_{\mathrm{DV}} < 15$ GeV region is used to define a symmetric uncertainty for this background component, as shown in Figure 5(a) and detailed in Section 7.

6.3 Alternative background estimate

Further validation of the estimate is performed with an alternative approach that aims to estimate each source of background independently. Data-driven techniques are used to build mass templates which describe the shape of m_{DV} from each specific background source, which are then normalized and combined into a complete background estimate.

Mass templates of merged vertices with varying track multiplicities are built by randomly merging pairs of DVs taken from different events in data. Only DVs with a distance significance of $S < 10$ are merged, where S is defined as the distance between vertices divided by its uncertainty. The mass templates are normalized by comparing the significance of the distance between pairs of DVs in the same event and in distinct events, as shown in Figure 6. The distribution of the distance significance taken from distinct events is normalized to match the distance significance distribution of DV pairs from the same event in the $S > 10$ region, where merging cannot occur. The deficit of DV pairs in the same event relative to DV pairs taken from distinct events in the $S < 10$ region is set as the overall normalization of the merged vertex mass template. In the assumption that the merging probability is small, this normalization procedure ensures that the difference of these two distributions is equal to the number of merged vertices expected [69]. To increase the number of available events for the determination of the normalization factor, only the cleaning requirements on track d_0-significance and the track p_{T} for tracks with $\Delta\phi_{\text{PV–DV}} < 0.2$ are applied. All other requirements are removed, as the quantities used in the selection criteria were found to have no correlation with the merging rate. The mass templates are built with the same loosened DV-track cleaning requirements, and the full DV-track cleaning is applied to the mass templates after they are normalized.

This background estimation method is sensitive to the presence of correlated DVs in the same event. Pairs of DVs are correlated if they originate from the same cascade hadronic interaction, for example. DVs which are correlated tend to be reconstructed close together with a small $\Delta\phi$, leading to an excess of DV pairs from the same event with a small distance significance between them. To evaluate the impact that correlated DVs have on this estimate, two sets of merged vertex mass templates for each track multiplicity of DVs are produced. The first set of templates is produced without a $\Delta\phi > 0.2$ selection, while the second set of templates is produced with the $\Delta\phi > 0.2$ selection. The nominal merged vertex background estimate is derived from the bin-by-bin average of the two sets of templates.

The contribution from high-mass DVs with an accidental crossing track is estimated as follows. Templates for (n+1)-track vertices are constructed by adding an accidental crossing track to n-track vertices from data. The accidental crossing track is drawn randomly from a collection of tracks reconstructed in data which have been incorrectly attached to a DV. The tracks are identified using displaced $K^0_{\text{S}} \to \pi^+\pi^-$ decays in data. To identify accidental crossing tracks, 3-track DVs where two of the tracks can be combined to form a vertex consistent with the K^0_{S} mass are identified. The third track in the vertex is added to the collection if it passes the DV-track cleaning. The track's p_{T}, η, and relative azimuthal angle to the direction of the PV-DV vector ($\Delta\phi$) are added to the collection. The (n+1)-track DV mass distribution is built by recalculating the mass of n-track DVs in data after attaching one additional track to it.

The behaviour of the accidental crossings background is expected to differ depending on the position of the DV in the fiducial volume. This is due to multiple factors, for example the vertexing reconstruction efficiency and the larger incident angles of tracks crossing DVs at large radii. Therefore this background estimate is evaluated separately in four radial detector regions[2], divided approximately by material structures in the inner detector volume within the fiducial region.

[2] The boundaries for these radial regions are at R = 0, 38, 120 and 300 mm.

The accidental crossing mass templates are normalized with a *crossing factor*, which is a measure of the probability that a DV is reconstructed with an unrelated track. The crossing factor is calculated by measuring the fraction of all $K^0_S \to \pi^+\pi^-$ decays reconstructed in data which have an accidentally crossing track. The number of K^0_S decays reconstructed without (with) an accidental crossing track is calculated using the mass spectrum of 2-track DVs (2-track combinations in 3-track DVs), shown in Figure 7. The mass spectrum is fit to a Gaussian distribution peak and a linear background. The linear background is subtracted from the mass spectrum and the number of entries in the mass spectrum within 40 MeV of the K^0_S mass gives the number of reconstructed $K^0_S \to \pi^+\pi^-$ decays. The level of non-K^0_S background in the K^0_S mass window is less than 10% in the 2-track DV mass spectra and ranges from 20–70% in the 3-track DV mass spectra, depending on the radial region.

In each radial region, two crossing factors are calculated. The first is dedicated to accidental crossings of selected tracks, which is required to estimate the contribution of n-track vertices with only one selected track that would otherwise fail to satisfy the DV selection criteria. The second considers all tracks and is used to estimate the contribution of n-track vertices with two or more selected tracks. In order to increase the number of reconstructed K^0_S decays available for these calculations, the innermost two radial regions are merged and a single set of crossing factors are calculated for both regions. The crossing factors, shown in Figure 8, range from 8.26×10^{-5} in the innermost radial region to 2.91×10^{-3} in the outermost radial region. The crossing factor increases at larger radii due to the decreasing vertex position resolution.

The component of background arising from hadronic interactions dominates in the low-mass region of the m_{DV} distribution. Therefore, to estimate this background in the signal region, the m_{DV} distribution is fit with an empirical function modelling the sharp increase below 2 GeV and follows an exponentially falling distribution in the high-mass region. The function is fitted to data in the $m_{\mathrm{DV}} < 10$ GeV region and extrapolated to the SRs with $m_{\mathrm{DV}} > 10$ GeV. Studies based on simulated events indicate that the contamination from background DVs originating from sources other than hadronic interactions in the $m_{\mathrm{DV}} < 10$ GeV region is expected to be negligible. There is a secondary component of hadronic interactions present in the high-m_{DV} region with a shallower exponential tail caused by the presence of elastic hadronic

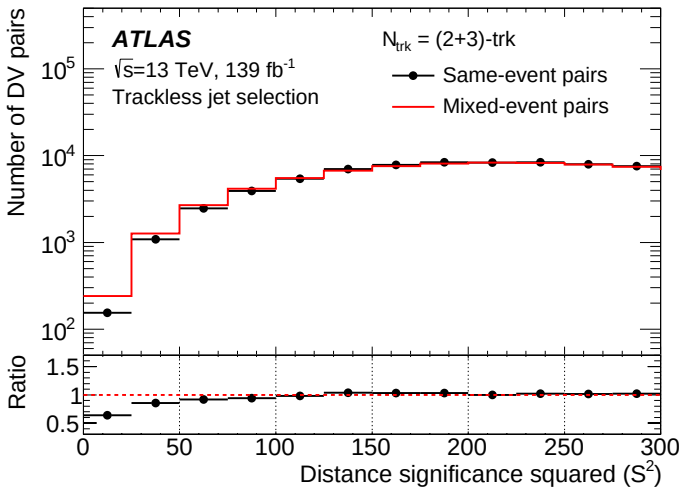

Figure 6: Squared significance of the distance between pairs of preselected DVs with two and three tracks, taken from the same event and from distinct events passing the Trackless jet selection. The mixed event distribution is normalized to match the same event distribution in the $S^2 > 100$ region.

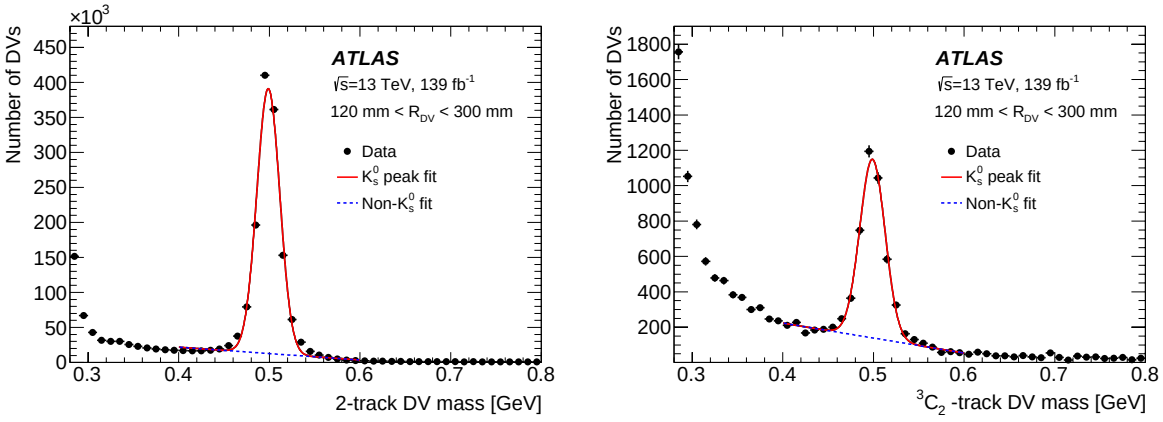

(a) (b)

Figure 7: The mass spectrum of preselected (a) 2-track DVs and (b) 2-track combinations of 3-track DVs ($^3C_2$) in one radial region. The mass spectrum is fit to a Gaussian function centered on the K^0_S mass and a linear background. The data in the K^0_S mass spectrum after subtracting the fitted background is used to compute the K^0_S crossing factors.

interactions, where the mass of the DV is dominated by a single track with small $\Delta\phi_{\text{PV–DV}}$. The difference between these exponential distribution tails is measured in simulated multijet events and used to apply a correction to the hadronic interactions template derived from data.

The normalized background estimates for the individual components are added to form a total expected background. The expected and observed event counts in the $n^{\text{DV}}_{\text{Tracks}} = 4$ sideband validation regions are shown in Figure 9. Good agreement is observed across the entire mass range.

The total expected background in the SR is calculated by integrating all $\geq$ 5-track mass templates in the $m_{\text{DV}} > 10$ GeV region, shown for the High-p_{T} jet and Trackless jet SRs in Table 3. The inclusive and component-based estimates are consistent within uncertainties, thereby providing a successful cross-check

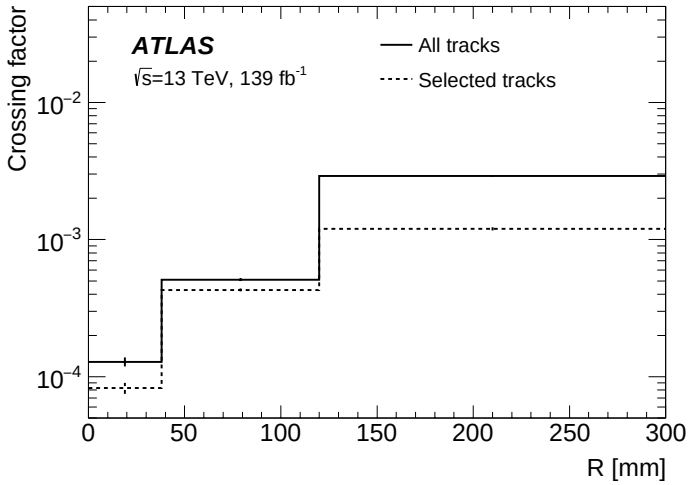

Figure 8: Crossing factors computed in each radial region. The bars show the statistical uncertainties.

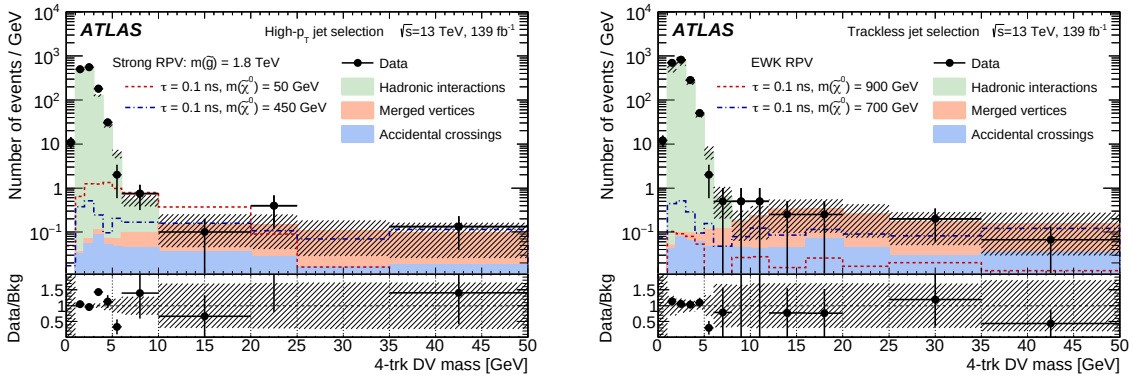

(a) (b)

Figure 9: The combined background predictions in events passing the (a) High-p_{T} jet selection and (b) Trackless jet selection 4-track DV validation regions. The overflow is included in the rightmost bin.

Table 3: The separate background estimates in the signal regions. The systematic uncertainties shown for each estimate are described in Section 7.2. The uncertainties on the combined background estimate are calculated assuming no correlation between the separate estimates. The rightmost column contains the background estimates from the inclusive method, described in Section 6.1.

Region	Merged vertices	Hadronic interactions	Accidental crossings	Combined	Inclusive
High-p_{T} jet SR	0.79 ± 0.66	0.006 ± 0.018	0.28 ± 0.21	1.08 ± 0.69	$0.46^{+0.27}_{-0.30}$
Trackless jet SR	1.5 ± 1.1	0.248 ± 0.077	0.32 ± 0.24	2.1 ± 1.1	$0.83^{+0.51}_{-0.53}$

of the inclusive background estimation technique. The inclusive method is chosen as the main method because it gives a smaller uncertainty and it has a more robust validation technique.

7 Uncertainties

In the following sections uncertainties derived for the inclusive background estimation, the alternative background estimate, and the expected signal yield are described.

7.1 Uncertainties in the inclusive background estimation

The systematic uncertainties associated with the background estimate are evaluated for each SR selection. Four sources of uncertainty are taken into account. First, the statistical uncertainty in the number of events with a SR-like DV in the CR is propagated to the final estimate. A toy method is used which performs 10,000 pseudo-experiments. In each pseudo-experiment, the number of events in the CR with a SR-like DV is varied bin-by-bin within its statistical uncertainty and used to calculate a new jet-DV probability distribution and extrapolation factor f. The standard deviation of the background estimate from all statistically varied toy experiments is taken as an uncertainty in the final background estimate.

The uncertainty in the residual dependence of the jet-DV probability on the amount of jet activity in the event is estimated by computing a new jet-DV probability which is parameterized as a function of the number of track-jets in the event. No statistically significant dependence of the jet-DV probability as a function of the jet activity in the event was found. However, to estimate any residual dependence below the statistical accuracy, a new jet-DV probability is computed which is parameterized as a linear function of the number of track-jets in the event. The fitted parameters in the linear function are varied within their uncertainties and the resulting jet-DV probability is used to estimate the background in the signal region. The largest variation in the background estimates is taken as an uncertainty.

A third uncertainty is applied to account for the non-closure of the estimate in some of the validation regions. This method underestimates the number of DVs reconstructed inside of material in events which satisfy the High-p_{T} jet selection criteria, as shown in Figure 5(a). Studies of simulated background events and the alternative background estimate indicate that the validation region in which this non-closure is the largest (events containing a DV with $n^{\mathrm{DV}}_{\mathrm{Tracks}} \geq 5$ and 10 GeV $< m_{\mathrm{DV}} <$ 15 GeV reconstructed inside of material) are populated dominantly ($> 99\%$) with background DVs from hadronic interactions. The same methods indicate that the expected contribution of hadronic interactions in the High-p_{T} jet SR is very small ($< 1\%$), due largely to the material map veto and m_{DV} requirements. The ratio of observed to expected events in the validation region with the largest non-closure is assigned as an uncertainty in the hadronic interactions background component. To determine an uncertainty in the inclusive background in other regions, the uncertainty in the hadronic interactions background component is scaled by the expected contribution of hadronic interactions to the total background in each region. The expected contribution of hadronic interactions in each region is calculated using the alternative background estimate. This uncertainty covers the remaining discrepancies between observed and expected background in the validation regions shown in Figure 5(a). The resulting uncertainty assigned to the inclusive background in the High-p_{T} jet SR is 4%.

Lastly an uncertainty is assigned to account for differences in the pile-up distributions between events in the CR and events which pass the jet selections of the SR. Events in the CR are reweighted so that their pile-up distribution matches that of events passing the SR jet selections and the background estimate is re-evaluated. The difference between the background estimate with and without pile-up-reweighting is used to define a correction factor, which is applied to both the nominal background estimate and its uncertainties. Furthermore the magnitude of this correction factor is applied as an additional uncertainty to the nominal background estimate.

These uncertainties are assumed to be uncorrelated, and added in quadrature to estimate the total systematic uncertainty. The final estimate of background in the signal regions with their associated uncertainties is listed in Table 4.

7.2 Uncertainties in an alternative background estimate

The systematic uncertainties in the alternative background estimate described in Section 6.3 are evaluated as follows: the uncertainty associated with the contribution from accidental crossings is evaluated by comparing the extracted crossing factors and mass templates with those extracted from $\Lambda \rightarrow p\pi$ decays, and altering the jet selection when deriving the crossing factors. The largest difference between the resulting background estimate is taken as an uncertainty. The resulting uncertainty in the predicted accidental crossing contribution is 25% in both of the signal regions.

The estimate of the hadronic interaction background relies on the assumption that the related DV mass spectrum follows an exponential shape. In order to determine the uncertainty in the estimate via the

Table 4: Systematic uncertainties associated with the background estimate. The “CR statistical” uncertainty is the propagation of the statistical variations of the CR to the estimate, while the “Non-linearity” uncertainty refers to the residual dependence of the jet-DV probability on the amount of jet activity in the event. The “VR non-closure” is calculated from the non-closure of the estimate inside of material validation regions. The “Pile-up" uncertainty is calculated by reweighting events in the CR to match the pileup distribution of events in each SR.

Region	Uncertainty source			
	CR statistical	Non-linearity	VR non-closure	Pile-up
High-p_{T} jet SR	± 58%	$^{+10\%}_{-27\%}$	± 4%	± 5.9%
Trackless jet SR	± 58%	$^{+6.3\%}_{-17\%}$	–	± 20%

functional fit method, a multivariate Gaussian distribution of the fit parameters is created from the covariance matrix of the fit. Sets of parameters are randomly sampled from this distribution to create alternate curves. The uncertainty is determined as the standard deviation of the envelope of the alternate curves. This is added in quadrature with the uncertainty on the shape correction originating from statistical variations in the simulated multijet events. The uncertainty amounts to a 300% (30%) uncertainty on the predicted hadronic interaction yield in the High-p_{T} (Trackless) jet SR. The larger uncertainty on the estimate in the High-p_{T} jet SR is driven by the uncertainty in the fit parameters.

The uncertainty on the merging rate due to statistical fluctuations is propagated to the mass template and amounts to 40% (10%) for the High-p_{T} (Trackless) jet SR. Furthermore, the difference between two sets of templates with and without the $\Delta\phi$ selection and the nominal is taken as a systematic uncertainty. In the $m_{\mathrm{DV}} > 10$ GeV region, this uncertainty is 7.4% (20%) for 4-trk DVs and 15% (28%) for $\geq$ 5-trk DVs in events passing the Trackless (High-p_{T}) jet SR.

The uncertainties in each component are assumed to be uncorrelated and are added in quadrature to produce the final uncertainty in the total background estimate.

7.3 Uncertainties on expected signal yield

The uncertainty of the event yields predicted for signal scenarios is affected by several sources: uncertainties in tracking and vertex reconstruction, uncertainty in the ISR modelling in MC simulation, the jet energy scale and resolution, and uncertainty in the integrated luminosity of the data sample.

The uncertainty on the track reconstruction efficiency of standard tracking is determined to be approximately 1.7% [70]. In order to estimate the uncertainty on the track reconstruction efficiency of LRT, the radial distributions of secondary vertices from K^0_{S} decays are compared in data and Pythia multijet simulation for each data-taking year, after normalizing the two distributions by the number of vertices at low radii, where tracking efficiencies are well understood. The mismodelling of the reconstruction efficiency in MC simulation at large track impact parameter and large vertex radius is estimated in this comparison. The observed difference is added in quadrature with the standard track reconstruction efficiency uncertainty and then applied as a conservative per-track efficiency uncertainty to the tracks associated with displaced vertices in the signal samples. The effect on final event counts with a fully selected DV is determined to be between 14% and 17%.

The effect on the signal efficiency due to variations of the amount of simulated pileup interactions is negligible. In order to estimate the size of the uncertainty due to the QCD radiation modelling, the factorization, renormalization, and merging scales were varied in MadGraph5_aMC@NLO, as well as in the parton showering tunes and radiation tunes. This effect corresponds to an uncertainty of about 20% in the signal selection efficiency for electroweakino pair production signals with $m(\tilde{\chi}_1^0) < 500$ GeV and the uncertainty decreases for higher $m(\tilde{\chi}_1^0)$. The uncertainty was found to be negligible for the gluino pair production signals. The differences between results from the nominal and varied predictions samples are used as the systematic uncertainties.

Uncertainties in the jet energy scale and resolution for jets originating from displaced decays were studied with the help of the simulated signal samples. They were found to impact the event counts of the EWK RPV signal model up to 10% and were negligible for the Strong RPV signal model.

The impact of the systematic uncertainties affecting the signal yield in the two signal regions is summarized in Table 5.

Table 5: Summary of the impact of systematic uncertainties in the predicted yield for the signal scenarios considered. These uncertainties apply to both SRs used in the search.

Source of uncertainty	Relative impact signal yield [%]	
	Gluino pairs	Electroweakino pairs
Total	17 – 20	20 – 31
Tracking and vertex reconstruction	14 – 17	
ISR modelling in MC simulation	< 1	1 – 24
Jet energy scale and resolution	1	10
Integrated luminosity of data sample	1.7	

8 Results

No events are observed in the Trackless jet SR, while a single event is observed in the High-p_T jet SR. The observed event yields are in good agreement with the background-only expectations. The single event observed in the High-p_T jet SR contains seven selected jets with p_T above 90.8 GeV, and one selected DV. The DV has five tracks, $m_{DV} = 32.6$ GeV, and net electric charge of $-1e$.

Figure 10 shows the two-dimensional distributions of m_{DV} and n^{DV}_{Tracks} in events passing the High-p_T and Trackless jet selections in data and signal MC.

The predicted backgrounds and observed yields in the two signal regions are used simultaneously to set exclusion limits on the BSM signal models of interest. The exclusion limits are set using the CL_s prescription [71]. The exclusion limit setting is implemented in `pyhf` 0.6.3 [72, 73]. It is done using a two-bin fit, where the two bins correspond to the High-p_T and Trackless jet signal region, respectively. The uncertainties in the background prediction in the two SRs are considered fully uncorreleated. The uncertainties in the signal yields are taken as fully correlated, with the exception of the uncertainty in the integrated luminosity of the data sample, which is considered fully uncorreleated.

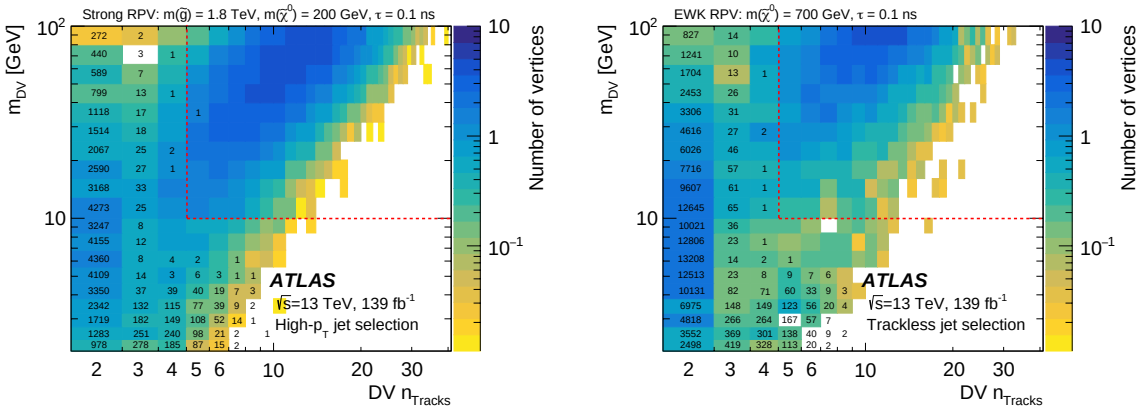

(a) (b)

Figure 10: Two-dimensional distribution of the invariant mass m_{DV} and the track multiplicity for preselected DVs in events which satisfy the (left) High-p_{T} and (right) Trackless jet selection requirements in data and signal MC. The shown numbers correspond to the observed vertex yields in data, while the colour-representation shows the expected signal yield of two benchmark models. The dashed line represents the boundary of the signal region requirements.

The expected and observed 95% CL exclusion limits on the mass of a long-lived pure-higgsino electroweakino triplet as a function of τ are shown in Figure 11. The expected and observed 95% CL exclusion limits on the mass and mean proper lifetime τ of a long-lived $\tilde{\chi}_1^0$ in gluino pair production events for a fixed $m(\tilde{g}) = 2400$ GeV are shown in Figure 12. For a mean proper lifetime of 0.1 ns, masses below $m(\tilde{\chi}_1^0) \simeq 1.58$ TeV are excluded independently of the presence of a heavier gluino. The observed limit extends above $m(\tilde{\chi}_1^0) = 1.5$ TeV for a range of mean proper lifetimes between 0.03 ns and 1 ns. Stronger limits can be set when the $\tilde{\chi}_1^0$ is produced in the decay of a heavier $\tilde{g}$. For $\tilde{\chi}_1^0$ masses on the order of few hundred GeV and below, the sensitivity decreases because of the sizeable Lorentz boost and the limited fiducial volume.

In Figure 13, the 95% CL upper limits on the production cross-section of electroweakino pairs in the EWK RPV model and gluino pairs in the Strong RPV model are shown as a function of $m(\tilde{\chi}_1^0)$. The limited variation as a function of $m(\tilde{\chi}_1^0)$ in the EWK RPV model is because the signal acceptance and efficiency are relatively invariant in $m(\tilde{\chi}_1^0)$ for the range considered here. For $\tau = 0.1$ ns, cross-section upper limits set are below 40 ab in the Strong RPV model and below 70 ab in the EWK RPV model.

Model-independent upper limits at 95% CL on the number of BSM events in the signal region are also derived, assuming no significant contamination from alternate signal models in the CRs used to derive the background predictions. Normalizing these limits by the integrated luminosity of the data sample, these numbers can be interpreted as upper limits on the visible BSM cross-section, denoted by σ_{vis}. This is defined as the product of signal acceptance, reconstruction efficiency, and production cross-section, and the results are given in Table 6. Parameterized signal acceptances and efficiences for the purpose of reinterpreting the results of this search are provided in a separate document [74].

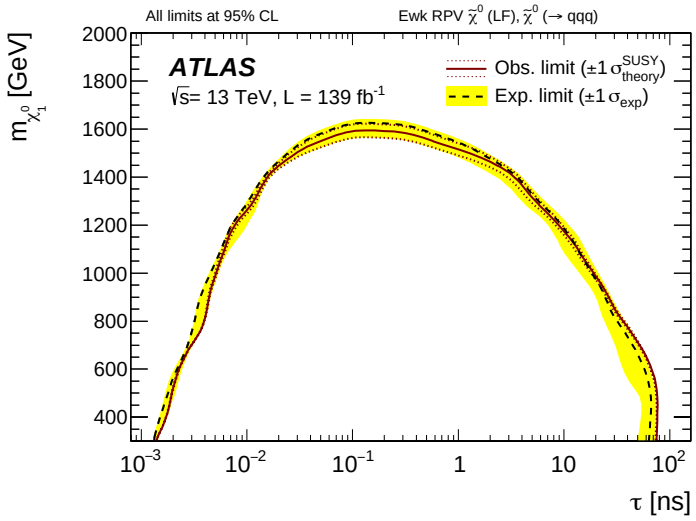

Figure 11: Exclusion limits at 95% CL on the lifetime and mass of the $\tilde{\chi}_1^0$ in electroweakino pair production models. The dashed line and the shaded band are the expected limit and its $\pm 1\sigma$ uncertainty, respectively. The thick solid line is the observed limit for the central value of the signal cross-section. The expected and observed limits do not include the effect of the theoretical uncertainties in the signal cross-section. The dotted lines show the effect on the observed limit of varying the signal cross-section by $\pm 1\sigma$ of the theoretical uncertainty. The area below the solid line is the excluded parameter space.

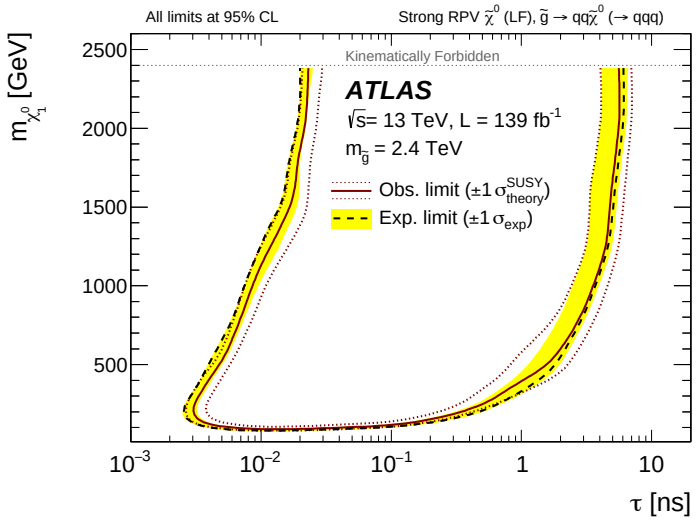

Figure 12: Exclusion limits at 95% CL on the lifetime and mass of the $\tilde{\chi}_1^0$ in gluino pair production models for a fixed $m(\tilde{g})$ = 2400 GeV. The dashed line and the shaded band are the expected limit and its $\pm 1\sigma$ uncertainty, respectively. The thick solid line is the observed limit for the central value of the signal cross-section. The expected and observed limits do not include the effect of the theoretical uncertainties in the signal cross-section. The dotted lines show the effect on the observed limit of varying the signal cross-section by $\pm 1\sigma$ of the theoretical uncertainty. The area between the two solid lines is the excluded parameter space.

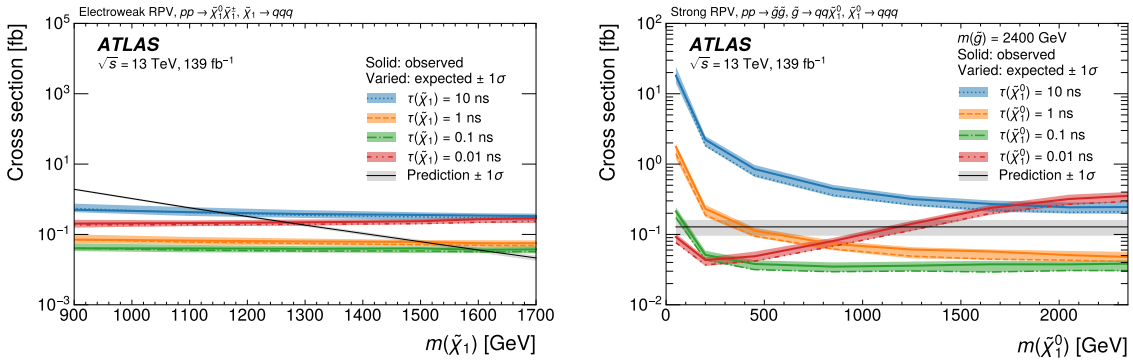

(a) (b)

Figure 13: Exclusion limits at 95% CL on the production cross section of (a) electroweakino pairs in the EWK RPV model and (b) gluino pairs in the Strong RPV model as a function of $m(\tilde{\chi}_1^0)$ are shown for several values of $\tau(\tilde{\chi}_1^0)$. The theoretical prediction of the signal production cross section and its uncertainty are shown in gray.

Table 6: The observed data, expected background, observed (S_{obs}^{95}) and expected (S_{exp}^{95}) limits on the number of signal events, and 95% CL upper limits on the visible cross section $\langle\sigma_{\text{vis}}\rangle_{\text{obs}}^{95}$.

Signal Region	Observed	Expected	S_{obs}^{95}	S_{exp}^{95}	$\langle\sigma_{\text{vis}}\rangle_{\text{obs}}^{95}$ [fb]
High-p_{T} jet SR	1	$0.46^{+0.27}_{-0.30}$	3.8	$3.1^{+1.0}_{-0.1}$	0.027
Trackless jet SR	0	$0.83^{+0.51}_{-0.53}$	3.0	$3.4^{+1.3}_{-0.3}$	0.022

9 Conclusion

A search for physics beyond the Standard Model giving rise to long-lived particle decays into hadrons is reported using the ATLAS experiment at the LHC using an accumulated data collection of 139 fb^{-1} of $\sqrt{s}$ = 13 TeV pp collisions. Event selections are developed to efficiently reject backgrounds. The yields expected from background in the two orthogonal signal regions used in the analysis are extracted from data. The data agree with the yields expected from the background-only hypothesis, with zero and one event passing the trackless and High-p_{T} jet SR requirements, respectively.

The results are interpreted in supersymmetric models with electroweakinos decaying via small values of the R-parity-violating couplings λ'' into quarks, giving the electroweakinos lifetimes τ in the ps to ns range. At 95% confidence level, $m(\tilde{\chi}_1^0)$ values up to 1.58 TeV for τ = 0.1 ns are excluded, independently of the presence of a heavier gluino. Upper limits on the visible cross-section for processes with the sought signature were also derived to be 0.03 fb and 0.02 fb for the High-p_{T} jet and Trackless jet SRs, respectively.

References

[1] L. Lee, C. Ohm, A. Soffer and T.-T. Yu,
Collider searches for long-lived particles beyond the Standard Model,
Progress in Particle and Nuclear Physics **106** (2019) 210, arXiv: 1810.12602.

[2] J. Alimena et al.,
Searching for long-lived particles beyond the Standard Model at the Large Hadron Collider,
Journal of Physics G: Nuclear and Particle Physics **47** (2020) 090501, arXiv: 1903.04497.

[3] M. J. Strassler and K. M. Zurek, *Echoes of a hidden valley at hadron colliders*,
Phys. Lett. B **651** (2007) 374, arXiv: hep-ph/0604261.

[4] N. Arkani-Hamed and S. Dimopoulos, *Supersymmetric unification without low energy supersymmetry and signatures for fine-tuning at the LHC*, JHEP **06** (2005) 073,
arXiv: hep-th/0405159.

[5] G. Giudice and A. Romanino, *Split supersymmetry*, Nucl. Phys. B **699** (2004) 65,
arXiv: hep-ph/0406088, Erratum: Nucl. Phys. B **706** (2005) 65.

[6] R. Barbier et al., *R-parity-violating supersymmetry*, Phys. Rept. **420** (2005) 1,
arXiv: hep-ph/0406039 [hep-ph].

[7] Y. Golfand and E. Likhtman,
Extension of the Algebra of Poincare Group Generators and Violation of P Invariance,
JETP Lett. **13** (1971) 323, [Pisma Zh. Eksp. Teor. Fiz. **13** (1971) 452].

[8] D. Volkov and V. Akulov, *Is the neutrino a goldstone particle?*, Phys. Lett. B **46** (1973) 109.

[9] J. Wess and B. Zumino, *Supergauge transformations in four dimensions*,
Nucl. Phys. B **70** (1974) 39.

[10] J. Wess and B. Zumino, *Supergauge invariant extension of quantum electrodynamics*,
Nucl. Phys. B **78** (1974) 1.

[11] S. Ferrara and B. Zumino, *Supergauge invariant Yang-Mills theories*, Nucl. Phys. B **79** (1974) 413.

[12] A. Salam and J. Strathdee, *Super-symmetry and non-Abelian gauges*, Phys. Lett. B **51** (1974) 353.

[13] N. Sakai, *Naturalness in supersymmetric GUTS*, Z. Phys. C **11** (1981) 153.

[14] S. Dimopoulos, S. Raby and F. Wilczek, *Supersymmetry and the scale of unification*,
Phys. Rev. D **24** (1981) 1681.

[15] L. E. Ibáñez and G. G. Ross, *Low-energy predictions in supersymmetric grand unified theories*,
Phys. Lett. B **105** (1981) 439.

[16] S. Dimopoulos and H. Georgi, *Softly broken supersymmetry and SU(5)*,
Nucl. Phys. B **193** (1981) 150.

[17] P. Fayet, *Supersymmetry and weak, electromagnetic and strong interactions*,
Phys. Lett. B **64** (1976) 159.

[18] P. Fayet,
Spontaneously broken supersymmetric theories of weak, electromagnetic and strong interactions,
Phys. Lett. B **69** (1977) 489.

[19] J. L. Goity and M. Sher, *Bounds on $\Delta B = 1$ couplings in the supersymmetric standard model*,
Physics Letters B **346** (1995) 69, arXiv: hep-ph/9412208.

[20] F. Zwirner, *Observable $\Delta B = 2$ transitions without nucleon decay in a minimal supersymmetric extension of the standard model*, Physics Letters B **132** (1983) 103, ISSN: 0370-2693.

[21] ATLAS Collaboration, *Search for displaced vertices arising from decays of new heavy particles in 7 TeV pp collisions at ATLAS*, Phys. Lett. B **707** (2012) 478, arXiv: 1109.2242 [hep-ex].

[22] ATLAS Collaboration, *Search for displaced muonic lepton jets from light Higgs boson decay in proton–proton collisions at $\sqrt{s}$ = 7 TeV with the ATLAS detector*, Phys. Lett. B **721** (2013) 32, arXiv: 1210.0435 [hep-ex].

[23] ATLAS Collaboration, *Search for massive, long-lived particles using multitrack displaced vertices or displaced lepton pairs in pp collisions at $\sqrt{s}$ = 8 TeV with the ATLAS detector*, Phys. Rev. D **92** (2015) 072004, arXiv: 1504.05162 [hep-ex].

[24] ATLAS Collaboration, *Search for long-lived, massive particles in events with a displaced vertex and a muon with large impact parameter in pp collisions at $\sqrt{s}$ = 13 TeV with the ATLAS detector*, Phys. Rev. D **102** (2020) 032006, arXiv: 2003.11956 [hep-ex].

[25] CMS Collaboration, *Search for long-lived particles decaying to jets with displaced vertices in proton–proton collisions at $\sqrt{s}$ = 13 TeV*, Phys. Rev. D **104** (2021) 052011, arXiv: 2104.13474 [hep-ex].

[26] CMS Collaboration, *Search for long-lived particles with displaced vertices in multijet events in proton–proton collisions at $\sqrt{s}$ = 13 TeV*, Phys. Rev. D **98** (2018) 092011, arXiv: 1808.03078 [hep-ex].

[27] ATLAS Collaboration, *The ATLAS Experiment at the CERN Large Hadron Collider*, JINST **3** (2008) S08003.

[28] B. Abbott et al., *Production and integration of the ATLAS Insertable B-Layer*, JINST **13** (2018) T05008, arXiv: 1803.00844 [physics.ins-det].

[29] ATLAS Collaboration, *Performance of the ATLAS trigger system in 2015*, Eur. Phys. J. C **77** (2017) 317, arXiv: 1611.09661 [hep-ex].

[30] ATLAS Collaboration, *The ATLAS Collaboration Software and Firmware*, ATL-SOFT-PUB-2021-001, 2021, URL: https://cds.cern.ch/record/2767187.

[31] ATLAS Collaboration, *ATLAS data quality operations and performance for 2015–2018 data-taking*, JINST **15** (2020) P04003, arXiv: 1911.04632 [physics.ins-det].

[32] ATLAS Collaboration, *Luminosity determination in pp collisions at $\sqrt{s}$ = 13 TeV using the ATLAS detector at the LHC*, ATLAS-CONF-2019-021, 2019, URL: https://cds.cern.ch/record/2677054.

[33] G. Avoni et al., *The new LUCID-2 detector for luminosity measurement and monitoring in ATLAS*, JINST **13** (2018) P07017.

[34] J. Alwall et al., *The automated computation of tree-level and next-to-leading order differential cross sections, and their matching to parton shower simulations*, JHEP **07** (2014) 079, arXiv: 1405.0301 [hep-ph].

[35] T. Sjöstrand et al., *An introduction to PYTHIA 8.2*, Comput. Phys. Commun. **191** (2015) 159, arXiv: 1410.3012 [hep-ph].

[36] R. D. Ball et al., *Parton distributions with LHC data*, Nucl. Phys. B **867** (2013) 244, arXiv: 1207.1303 [hep-ph].

[37] ATLAS Collaboration, *ATLAS Pythia 8 tunes to 7 TeV data*, ATL-PHYS-PUB-2014-021, 2014, URL: https://cds.cern.ch/record/1966419.

[38] L. Lönnblad, *Correcting the Colour-Dipole Cascade Model with Fixed Order Matrix Elements*, JHEP **05** (2002) 046, arXiv: hep-ph/0112284.

[39] L. Lönnblad and S. Prestel, *Matching tree-level matrix elements with interleaved showers*, JHEP **03** (2012) 019, arXiv: 1109.4829 [hep-ph].

[40] W. Beenakker et al., *Production of Charginos, Neutralinos, and Sleptons at Hadron Colliders*, Phys. Rev. Lett. **83** (1999) 3780, arXiv: hep-ph/9906298, Erratum: Phys. Rev. Lett. **100** (2008) 029901.

[41] J. Debove, B. Fuks and M. Klasen, *Threshold resummation for gaugino pair production at hadron colliders*, Nucl. Phys. B **842** (2011) 51, arXiv: 1005.2909 [hep-ph].

[42] B. Fuks, M. Klasen, D. R. Lamprea and M. Rothering, *Gaugino production in proton-proton collisions at a center-of-mass energy of* 8 *TeV*, JHEP **10** (2012) 081, arXiv: 1207.2159 [hep-ph].

[43] B. Fuks, M. Klasen, D. R. Lamprea and M. Rothering, *Precision predictions for electroweak superpartner production at hadron colliders with* RESUMMINO, Eur. Phys. J. C **73** (2013) 2480, arXiv: 1304.0790 [hep-ph].

[44] J. Fiaschi and M. Klasen, *Neutralino-chargino pair production at NLO+NLL with resummation-improved parton density functions for LHC Run II*, Phys. Rev. D **98** (2018) 055014, arXiv: 1805.11322 [hep-ph].

[45] C. Borschensky et al., *Squark and gluino production cross sections in pp collisions at* $\sqrt{s} = 13, 14, 33$ *and* 100 *TeV*, Eur. Phys. J. C **74** (2014) 3174, arXiv: 1407.5066 [hep-ph].

[46] W. Beenakker, C. Borschensky, M. Krämer, A. Kulesza and E. Laenen, *NNLL-fast: predictions for coloured supersymmetric particle production at the LHC with threshold and Coulomb resummation*, JHEP **12** (2016) 133, arXiv: 1607.07741 [hep-ph].

[47] W. Beenakker et al., *NNLL resummation for squark and gluino production at the LHC*, JHEP **12** (2014) 023, arXiv: 1404.3134 [hep-ph].

[48] W. Beenakker et al., *Towards NNLL resummation: hard matching coefficients for squark and gluino hadroproduction*, JHEP **10** (2013) 120, arXiv: 1304.6354 [hep-ph].

[49] W. Beenakker et al., *NNLL resummation for squark-antisquark pair production at the LHC*, JHEP **01** (2012) 076, arXiv: 1110.2446 [hep-ph].

[50] W. Beenakker et al., *Soft-gluon resummation for squark and gluino hadroproduction*, JHEP **12** (2009) 041, arXiv: 0909.4418 [hep-ph].

[51] A. Kulesza and L. Motyka, *Soft gluon resummation for the production of gluino-gluino and squark-antisquark pairs at the LHC*, Phys. Rev. D **80** (2009) 095004, arXiv: 0905.4749 [hep-ph].

[52] A. Kulesza and L. Motyka, *Threshold Resummation for Squark-Antisquark and Gluino-Pair Production at the LHC*, Phys. Rev. Lett. **102** (2009) 111802, arXiv: 0807.2405 [hep-ph].

[53] W. Beenakker, R. Höpker, M. Spira and P. Zerwas, *Squark and gluino production at hadron colliders*, Nucl. Phys. B **492** (1997) 51, arXiv: hep-ph/9610490.

[54] J. Butterworth et al., *PDF4LHC recommendations for LHC Run II*, J. Phys. G **43** (2016) 023001, arXiv: 1510.03865 [hep-ph].

[55] ATLAS Collaboration, *The Pythia 8 A3 tune description of ATLAS minimum bias and inelastic measurements incorporating the Donnachie–Landshoff diffractive model*, ATL-PHYS-PUB-2016-017, 2016, URL: https://cds.cern.ch/record/2206965.

[56] A. D. Martin, W. J. Stirling, R. S. Thorne and G. Watt, *Parton distributions for the LHC*, Eur. Phys. J. C **63** (2009) 189, arXiv: 0901.0002 [hep-ph].

[57] ATLAS Collaboration, *The ATLAS Simulation Infrastructure*, Eur. Phys. J. C **70** (2010) 823, arXiv: 1005.4568 [physics.ins-det].

[58] GEANT4 Collaboration, S. Agostinelli et al., *GEANT4 – a simulation toolkit*, Nucl. Instrum. Meth. A **506** (2003) 250.

[59] ATLAS Collaboration, *Performance of the reconstruction of large impact parameter tracks in the inner detector of ATLAS*, ATL-PHYS-PUB-2017-014, 2017, URL: https://cds.cern.ch/record/2275635.

[60] ATLAS Collaboration, *Vertex Reconstruction Performance of the ATLAS Detector at* $\sqrt{s} = 13$ *TeV*, ATL-PHYS-PUB-2015-026, 2015, URL: https://cds.cern.ch/record/2037717.

[61] ATLAS Collaboration, *Performance of vertex reconstruction algorithms for detection of new long-lived particle decays within the ATLAS inner detector*, ATL-PHYS-PUB-2019-013, 2019, URL: https://cds.cern.ch/record/2669425.

[62] ATLAS Collaboration, *Muon reconstruction and identification efficiency in ATLAS using the full Run 2 pp collision data set at* $\sqrt{s} = 13$ *TeV*, Eur. Phys. J. C **81** (2021) 578, arXiv: 2012.00578 [hep-ex].

[63] ATLAS Collaboration, *Electron reconstruction and identification in the ATLAS experiment using the 2015 and 2016 LHC proton–proton collision data at* $\sqrt{s} = 13$ *TeV*, Eur. Phys. J. C **79** (2019) 639, arXiv: 1902.04655 [hep-ex].

[64] ATLAS Collaboration, *Properties of jets and inputs to jet reconstruction and calibration with the ATLAS detector using proton–proton collisions at* $\sqrt{s} = 13$ *TeV*, ATL-PHYS-PUB-2015-036, 2015, URL: https://cds.cern.ch/record/2044564.

[65] M. Cacciari, G. P. Salam and G. Soyez, *The anti-*k_t *jet clustering algorithm*, JHEP **04** (2008) 063, arXiv: 0802.1189 [hep-ph].

[66] M. Cacciari, G. P. Salam and G. Soyez, *FastJet user manual*, Eur. Phys. J. C **72** (2012) 1896, arXiv: 1111.6097 [hep-ph].

[67] ATLAS Collaboration, *Jet energy scale measurements and their systematic uncertainties in proton–proton collisions at* $\sqrt{s} = 13$ *TeV with the ATLAS detector*, Phys. Rev. D **96** (2017) 072002, arXiv: 1703.09665 [hep-ex].

[68] ATLAS Collaboration, *Selection of jets produced in* 13 *TeV proton–proton collisions with the ATLAS detector*, ATLAS-CONF-2015-029, 2015, URL: https://cds.cern.ch/record/2037702.

[69] ATLAS Collaboration, *Charged-particle distributions in* $\sqrt{s} = 13$ *TeV pp interactions measured with the ATLAS detector at the LHC*, Phys. Lett. B **758** (2016) 67, arXiv: 1602.01633 [hep-ex].

[70] ATLAS Collaboration,
Early Inner Detector Tracking Performance in the 2015 Data at $\sqrt{s} = 13$ *TeV*,
ATL-PHYS-PUB-2015-051, 2015, URL: https://cds.cern.ch/record/2110140.

[71] A. L. Read, *Presentation of search results: the* CL_S *technique*, J. Phys. G **28** (2002) 2693.

[72] L. Heinrich, M. Feickert, G. Stark and K. Cranmer,
pyhf: pure-Python implementation of HistFactory statistical models,
Journal of Open Source Software **6** (2021) 2823, arXiv: 2211.15838.

[73] G. Cowan, K. Cranmer, E. Gross and O. Vitells,
Asymptotic formulae for likelihood-based tests of new physics, Eur. Phys. J. C **71** (2011) 1554,
arXiv: 1007.1727 [physics.data-an], Erratum: Eur. Phys. J. C **73** (2013) 2501.

[74] ATLAS Collaboration, *Search for long-lived, massive particles in events with displaced vertices and multiple jets in* pp *collisions at* $\sqrt{s} = 13$ *TeV with the ATLAS detector*,
https://doi.org/10.17182/hepdata.137762, HEPData (collection), 2023.